**ORIGINAL PAPER**

CrossMark

# Use of multi-source remote sensing images to describe the sudden Shanshucao landslide in the Three Gorges Reservoir, China

Haifeng Huang [1,2,3] · Kun Song [2,3,4] · Wu Yi [3,4] · Jingjing Long [2,3] · Qing Liu [2,3] · Guodong Zhang [3,4]

## Abstract

The primary objective of this research is to better understand the movement characteristics and patterns of a sudden landslide that occurred in the Three Gorges Reservoir, China (the Sept. 2, 2014 Shanshucao landslide) by using three periods of multi-source remote sensing images in combination with a field survey. A georeferenced, aerophotographic orthomosaic and corresponding 1:2000 topographic map of the pre-landslide area was referenced to rectify the micro-unmanned aerial vehicle (UAV) based orthomosaic, digital surface model (DSM) and Google Earth satellite image of the post-landslide area. By using orthomosaics of the post-landslide area, especially the very high spatial resolution micro-UAV based orthomosaic, the landslide boundaries were accurately delineated. By comparing the images of the area both pre- and post-landslide, three landslide subzones were identified, and two boundaries between the three subareas were divided more precisely than in previous studies. Based on the digital elevation model (DEM) of the pre-landslide area and DSM of the post-landslide area, the change in altitude and volume of the landslide were quantified. Then, the movement pattern of the landslide was proposed. The results showed the rocky, southern sliding part was the main sliding zone with the longest distance and deepest sliding surface, and the northern soil mass did not experience any overall movement. However, loose soil mass collapse and features of counterclockwise rotation were observed under the traction of the rocky, southern sliding part. Additionally, more accurate knowledge has been obtained including the location of the original lateral boundary, shear outlet altitudes, and main triggering factors of the rocky sliding mass. This study has demonstrated that the use of multi-source remote sensing images, which include both pre- and post-landslide images, can effectively describe the characteristics, patterns, and even the mechanism of a sudden landslide.

**Keywords** Sudden landslide · Remote sensing image · Orthomosaic · Movement pattern · Three Gorges Reservoir

✉ Kun Song
songkun_ctgu@163.com

1 Hubei Key Laboratory of Intelligent Vision Based Monitoring for Hydroelectric Engineering, China Three Gorges University, Yichang 443002, China

2 Hubei Key Laboratory of Disaster Prevention and Mitigation, China Three Gorges University, Yichang 443002, China

3 National Field Observation and Research Station of Landslides in The Three Gorges Reservoir Area of Yangtze River, China Three Gorges University, Yichang 443002, China

4 Collaborative Innovation Center for Geo-Hazards and Eco-Environment in The Three Gorges Area of Hubei Province, Yichang 443002, China

## Introduction

In the forecasting, prevention, and mitigation of landslides, it is extremely important to observe the movement process, assess behavior of a landslide, and identify its deformation mechanism (Petley et al. 2002). Currently, many deformation monitoring techniques such as a global positioning system (GPS) (Huang et al. 2014; Macciotta et al. 2016), inclinometers (Stark and Choi 2008), extensometry (Chung et al. 2016), robotic total station (Manconi and Giordan 2016), ground-based interferometric synthetic aperture radar (GB InSAR) (Carlà et al. 2017), differential interferometry synthetic aperture radar (DInSAR) (De Novellis et al. 2016), laser scanning (Kasperski et al. 2010), and unmanned aerial vehicle (UAV) based remote sensing (Niethammer et al. 2012) have been used to follow the movements of landslides that exhibit creep. However, sudden landslides are usually characterized by rapid failure that cannot be predicted or even detected in advance.

Thus, these landslides often resulted in significant casualties and property damage, e.g., the well-known Qianjiangping landslide, which occurred at 00:20 on July 14, 2003 in the Three Gorges Reservoir, China shortly after the water level increased to 135 m; this landslide destroyed four factories and 346 houses, claimed 24 lives, left 1200 people homeless, and led to direct economic losses of approximately 7 million USD (Wang et al. 2004; Jian et al. 2014). In addition, a lack of monitoring data for sudden landslides makes it very difficult to accurately understand the movement characteristics, processes, mechanisms, and laws. Thus, this lack of understanding does not assist in increasing knowledge or experience to prevent the recurrence of similar disasters. The Shanshucao landslide that occurred on Sept. 2, 2014 (Huang et al. 2015; Xu et al. 2015), which is studied in this paper, was only 1.5 km away from the Qianjiangping landslide, and while there were many similarities between them, this landslide was not predicted.

With the rapid development of remote sensing technology, the use of a variety of sensors could provide a wealth of high-resolution remote sensing data to help us to understand the Earth's surface and its changes in detail from a macro perspective (Tofani et al. 2013). Therefore, if the images and terrain data from pre- and post-landslide areas are obtained, the deformation and failure process of a sudden landslide might be revealed. In fact, even some deformation characteristics or laws, which have not yet been discovered or are prone to neglect when using ground-based monitoring techniques such as GPS, might be revealed, and thus this provides valuable knowledge for the prevention of similar disasters.

In this study, three periods of high-resolution images and two terrain datasets of the Shanshucao area, both pre- and post-landslide in the Three Gorges Reservoir, were collected and combined with a field survey to better analyze and understand the sliding characteristics and patterns of a sudden landslide occurrence.

## The Shanshucao landslide

The Shanshucao landslide occurred on the west bank of the Luogudong River, which is a secondary tributary of the Yangtze River in Zigui County, Hubei Province of central China (Xu et al. 2015) and is approximately 47 km from the Three Gorges Dam (Fig. 1 a, b). It was located near the town of Shazhenxi, which was only 300 m from a junior middle school. In addition, the Qianjiangping landslide was approximately 1.5 km to the northwest (Fig. 1 b, c), and this landslide occurred on July 13, 2003, which caused extensive damage with many casualties (Wang et al. 2004; Jian et al. 2014).

The Shanshucao landslide occurred at 13:19 on Sept. 2, 2014, and the entire slide lasted approximately 2 min (Huang et al. 2015). A small local hydropower station including power

houses, pressure pipes, an impounding forebay, and a 5-story dormitory were destroyed (Fig. 1 d). In addition, 160 m of national highway (G348) was interrupted, and an area of approximately 0.2 million $m^2$ of citrus trees was seriously damaged (Huang et al. 2015; Xu et al. 2015). Fortunately, there were no fatalities in this event because the local residents reported clues of slope deformation in a timely manner; then, the landslide specialists and governmental officials made a prompt collaborative decision to evacuate all relevant personnel before the failure occurred (Huang et al. 2015).

The landslide had an average width of 130 m in the north-south direction and average length of 300 m in the west-east direction. The landslide extends eastward from the head close to a county road and downslope to the toe area on the banks of the Luogudong River at an altitude of 145–285 m. The entire planar area is approximately $39 \times 10^3$ $m^2$. According to field investigations and related studies, the Shanshucao landslide was composed of two parts: the southern main rock sliding mass and northern secondary soil sliding mass (Fig. 2). The rock sliding part had a length of 329 m, an average width of 60 m, and a planar area of approximately $20 \times 10^3$ $m^2$; and the soil sliding part had a length of 270 m, an average width of 70 m, and a planar area of approximately $19 \times 10^3$ $m^2$.

Lithologically, the bedrock belongs to the Qianfoya Formation of Middle Jurassic Age ($J_2q$), which consists of thick layered sandstones with interbedded thin to medium layered, silty mudstones. The attitude of the bedrock varies from 120–124°/19–21°; that is, the landslide developed on a consequent slope. The Quaternary strata include an eluvial and diluvial layer ($Q_4^{el+dl}$), which mostly consists of sandy clay with sandstone debris, and the accumulation of the landslide ($Q_4^{del}$). The engineering survey showed that the bedrock was exposed on the south side of the landslide along the river bank and a local area on the north side; the $Q_4^{el+dl}$ was mainly found on the northwest to north side of the landslide (Fig. 2). Figure 3 shows the longitudinal section sketch (line 1–1′ in Fig. 2) of the main rock sliding part of the landslide. Two obvious silty mudstone layers were found in the thick sandstone layers, and the top surface of the lower mudstone layer formed the main slip surface of the rock mass.

Although the local residents found some clues of the landslide failure a few hours in advance, no obvious or long-term signs of creeping deformation were observed, i.e., the occurrence of the Shanshucao landslide was sudden. In addition, the main southern part was rocky, and the secondary northern part was soil; consequently, different characteristics and movement patterns existed even during the same landslide process (Huang et al. 2015; Xu et al. 2015), e.g., a deep trough with overhanging cliffs was formed in the southern part (Figs. 1d, 3), whereas a disturbed loose soil mass and cracks were left in the northern part. The Shanshucao landslide was a sudden occurrence geohazard with a complicated and elusive movement process.

**Fig. 1** Location and general overview of the Shanshucao landslide. **a** Location in China; **b** location in the Three Gorges Reservoir; **c** location in the town of Shazhenxi; and **d** general view of the southern rocky part of the failed landslide

## Methods

### Multi-source remote sensing images

To understand the sudden movement characteristics and patterns of the Shanshucao landslide, three periods (one pre-landslide and two post-landslide) of high-resolution images and terrain data were collected (Table 1, Fig. 4) as follows:

(1) Georeferenced, aerophotographic orthomosaic with an approximately 20 cm ground sampling distance (GSD) (Fig. 4 a) and corresponding 2009 1:2000 topographic map. These unique image and terrain data of the pre-

landslide had high absolute planar and altitude accuracy; simultaneously, they were used as reference data to establish ground control points (GCPs) to register other images and terrain data.

(2) Georeferenced satellite image with an approximate 1 m GSD for Dec. 17, 2014, which was obtained from Google Earth (Fig. 4b). Although the image had a relatively low spatial resolution and relatively high shading, it differed significantly from the other images with respect to texture and color. This image could more accurately reflect the surface features (especially the sliding soil mass) of the post-landslide area, because the image was captured in winter after only three months, and the
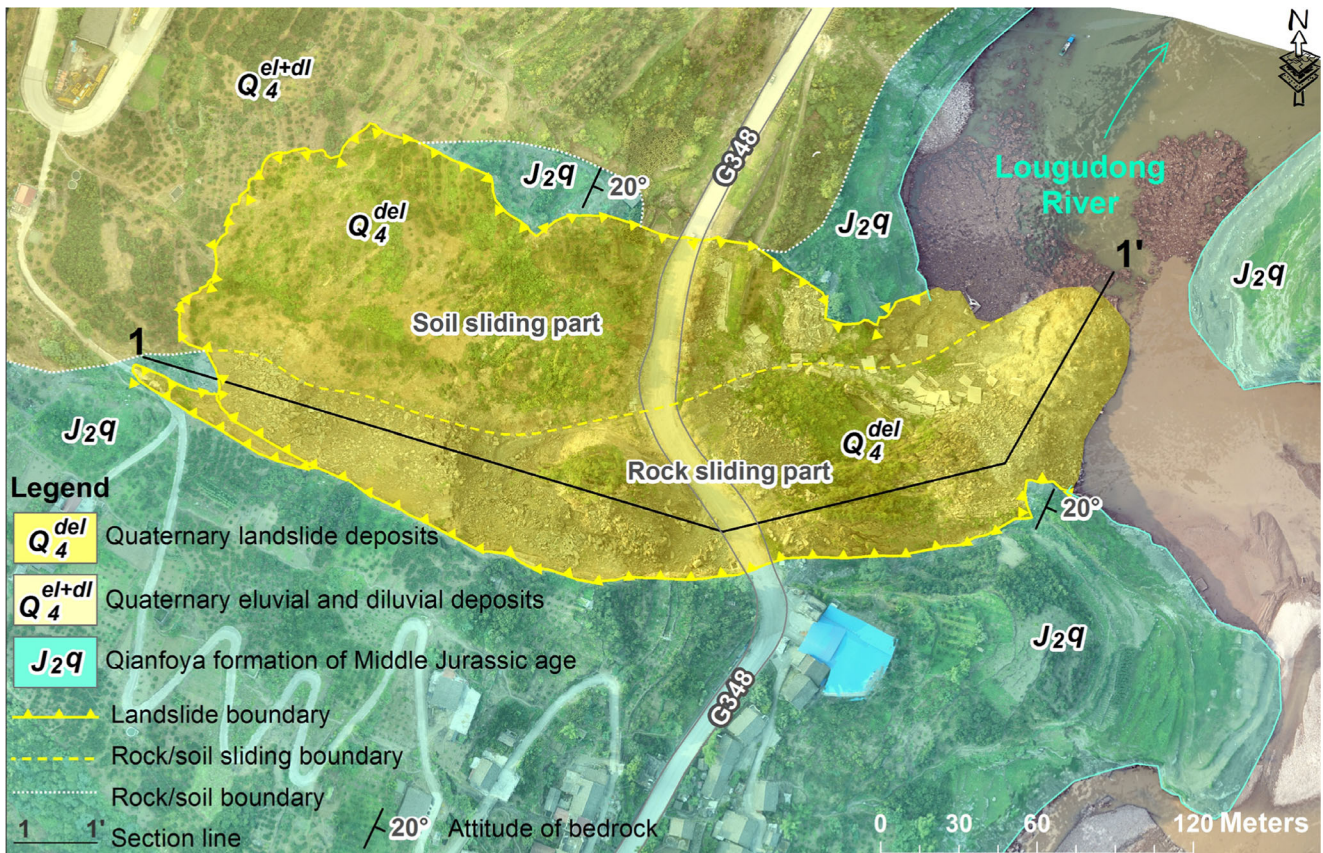
Fig. 2 Simplified geological map of the Shanshucao landslide. The base map is the micro-UAV based orthomosaic for June 19, 2015

sliding soil mass surface had not yet been changed by replanting.

(3) Georeferenced orthomosaic (Fig. 4c) and digital surface model (DSM) with 3.6 cm GSD, which was captured by a micro-UAV system (Fig. 5) on June 19, 2015, and generated by photogrammetry (Westoby et al. 2012;

Colomina and Molina 2014). The very high spatial resolution orthomosaic and DSM of the post-landslide area can provide more accurate information on the planar and vertical changes of the landslide compared with the aerophotographic orthomosaic and terrain data of the pre-landslide area.
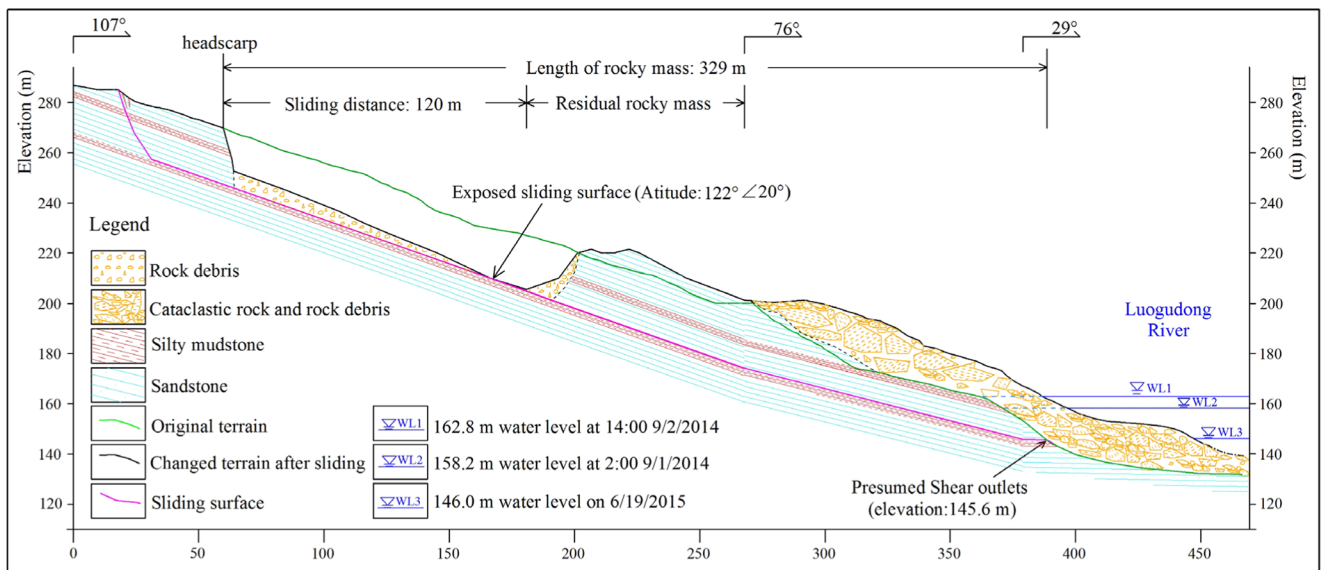


Fig. 3 The longitudinal section sketch (line 1–1′ in Fig. 2) of the main rocky part of the Shanshucao landslide

**Table 1** Characteristics of multi-source remote sensing images and terrain data pertaining to the Shanshucao landslide

| Image features | Shanshucao landslide (13:19, Sept. 2, 2014) | | |
| --- | --- | --- | --- |
| | Pre-landslide | Post-landslide | |
| Type | Georeferenced aerophotographic orthomosaic | Georeferenced satellite image | Georeferenced orthomosaic |
| Date | Unknown date in 2009 | Dec. 17, 2014 | June 19, 2015 |
| Source | Aerophotography | Google Earth | Micro-UAV |
| GSD | Approximately 20 cm | Approximately 1 m | 3.6 cm |
| Corresponding terrain data | Topographic map (1:2000) | No | DSM |

**Fig. 4** Three periods of multi-source remote sensing images of the Shanshucao landslide. **a** aerophotographic orthomosaic of the pre-landslide area in 2009; **b** satellite image of the post-landslide area on Dec. 17, 2014, which was obtained from Google Earth; and **c** micro-UAV based orthomosaic of the post-landslide area on June 19, 2015



(a) Pre-landslide in 2009

(b) Post-landslide on Dec. 17, 2014

(c) Post-landslide on Jun. 19, 2015

**Fig. 5** The micro-UAV that was used to capture photos and generate georeferenced orthomosaic and DSM of the post-landslide area on June 19, 2015

## Image registration

High-precision image registration is a prerequisite for detecting changes between an area pre- and post-landslide (Martha et al. 2010; Immerzeel et al. 2014; Turner et al. 2015). Due to the high absolute planar and altitude accuracy, the georeferenced aerophotographic orthomosaic and corresponding 2009 1:2000 topographic map were used as references to rectify the micro-UAV based orthomosaic, DSM, and the satellite image of the post-landslide area obtained from Google Earth as follows:

(1) Georeferencing of micro-UAV based orthomosaic and DSM on June 19, 2015.

Although all original photos collected by the micro-UAV contained GPS data, the addition of GCPs can significantly increase the absolute accuracy of the generated orthomosaic and DSM by photogrammetry (Niethammer et al. 2012; Lucieer et al. 2014; Huang et al. 2017b). Therefore, 25 GCPs including a house corner, pool corner, highway intersection, stable rock, etc., were carefully selected. It is worth noting that all GCPs could be easily identified on both the aerophotographic orthomosaic of the pre-landslide area and the original photos collected by the micro-UAV; however, the GCPs were located outside the landslide and on an immovable area (i.e., both the planar location and vertical altitude were unchanged). Then, the three-dimensional (3D) coordinates of all GCPs were obtained using geographic information system (GIS) software, i.e., the planar $XY$ coordinates were extracted from the 2009 georeferenced, aerophotographic orthomosaic, and the vertical altitude $Z$ value was extracted from the digital elevation model (DEM) with a 1-m GSD that was generated based on the contours of the 2009 1:2000 topographic map. Finally, all 25 3D GCPs

were used to georeference and rectify the micro-UAV based orthomosaic and DSM on June 19, 2015 by means of photogrammetry. Because all GCP coordinates that were used to generate the micro-UAV based orthomosaic and DSM on June 19, 2015 originated from the 2009 georeferenced images and terrain data, the georeferencing and rectifying process for the micro-UAV based data was actually an image registration process using the 2009 georeferenced data (Huang et al. 2017a).

(2) Georeferencing of the satellite image for Dec. 17, 2014 obtained from Google Earth.

On Google Earth, two mosaic images of the Shanshucao landslide area could be found, which were taken on Dec. 17, 2014 and Sept. 29, 2015, respectively. Only the image of Dec. 17, 2014 was used for the analysis of the sliding soil mass surface features, because it had a shorter time interval to the landslide occurrence. Then, due to the offset and distortion of Google Earth images, registering the Dec. 17, 2014 mosaic image with the georeferenced aerophotographic orthomosaic was necessary. Similarly, eight 2D GCPs with the same features as the 25 3D GCPs mentioned above were carefully selected, and their $XY$ coordinates were extracted from the 2009 georeferenced aerophotographic orthomosaic. Finally, based on these 2D GCPs, 2nd order polynomial transformation was carried out to rectify and register the Dec. 17, 2014 satellite image obtained from Google Earth by using the *Georeferencing* tool in ArcGIS.

## Landslide characteristics and pattern analysis

The use of registered, multi-source remote sensing images and terrain data (DEM or DSM) of the area pre- and post-landslide contributed to the analysis and understanding of the sliding characteristics and patterns of the sudden Shanshucao landslide.

First, based on the orthomosaics of the post-landslide area, especially the micro-UAV based orthomosaic with a very high spatial resolution (3.6 cm GSD; Fig. 4 c), landslide boundaries were accurately delineated and combined with the field survey. Some landslide characteristics pertaining to the boundary, sliding mass, etc., were analyzed, which could help to understand the sliding patterns.

Then, based on the pre- and post-landslide orthomosaics, by comparing the location change of some easy-to-identify objects, such as the impounding forebay, retaining wall, dormitory, etc., the movement characteristics including mainly the sliding distance and direction could be quantified.

In addition, based on the DEM of the pre-landslide area and the DSM of the post-landslide area, calculating the difference between the two terrain data values allowed the change in altitude and volume to be quantified.

**Table 2** Summary of spatial errors between the pre- and post-landslide remote sensing results

| Data | GCPs (used as check points) | | | |
|---|---|---|---|---|
| | Number | $X_{RMSE}$ (m) | $Y_{RMSE}$ (m) | $Z_{RMSE}$ (m) |
| Micro-UAV based orthomosaic and DSM from June 19, 2015 | 25 | 0.133 | 0.123 | 0.323 |
| Dec. 17, 2014 satellite image from Google Earth | 8 | 0.204 | 0.259 | / |

Finally, by combining the above analysis results, the sliding characteristics and patterns of the Shanshucao landslide were revealed.

## Results

### Accuracy of image registration

The 25 GCPs were used as check points to assess the accuracy of the micro-UAV based orthomosaic and DSM on June 19, 2015, and eight GCPs were used to assess the accuracy of the Dec. 17, 2014 Google Earth satellite image. The root mean square errors (RMSEs) of the corresponding check points were also calculated (Table 2).

The absolute position errors of the micro-UAV based orthomosaic and DSM were approximately 0.13 m in the horizontal direction ($X$, $Y$) and 0.32 m in the vertical direction ($Z$). The registration errors of the satellite image from Google Earth were approximately 0.20 m and 0.26 m in the $X$ and $Y$ directions, respectively. The results indicated a sub-meter level registration accuracy, which was acceptable for the analysis of the characteristics and patterns of the Shanshucao landslide.
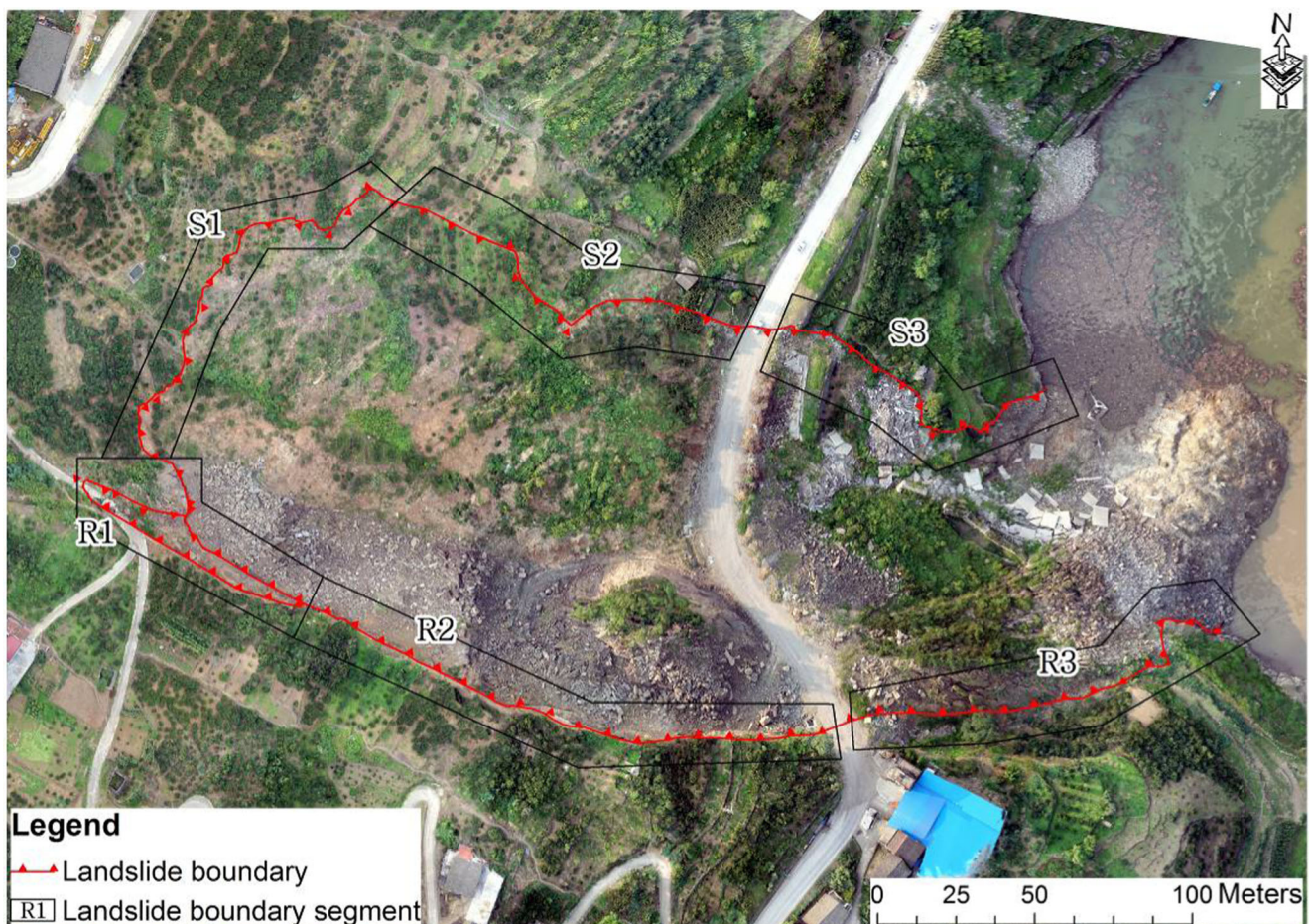


**Fig. 6** Boundary of the Shanshucao landslide; the base map is the micro-UAV based orthomosaic from June 19, 2015
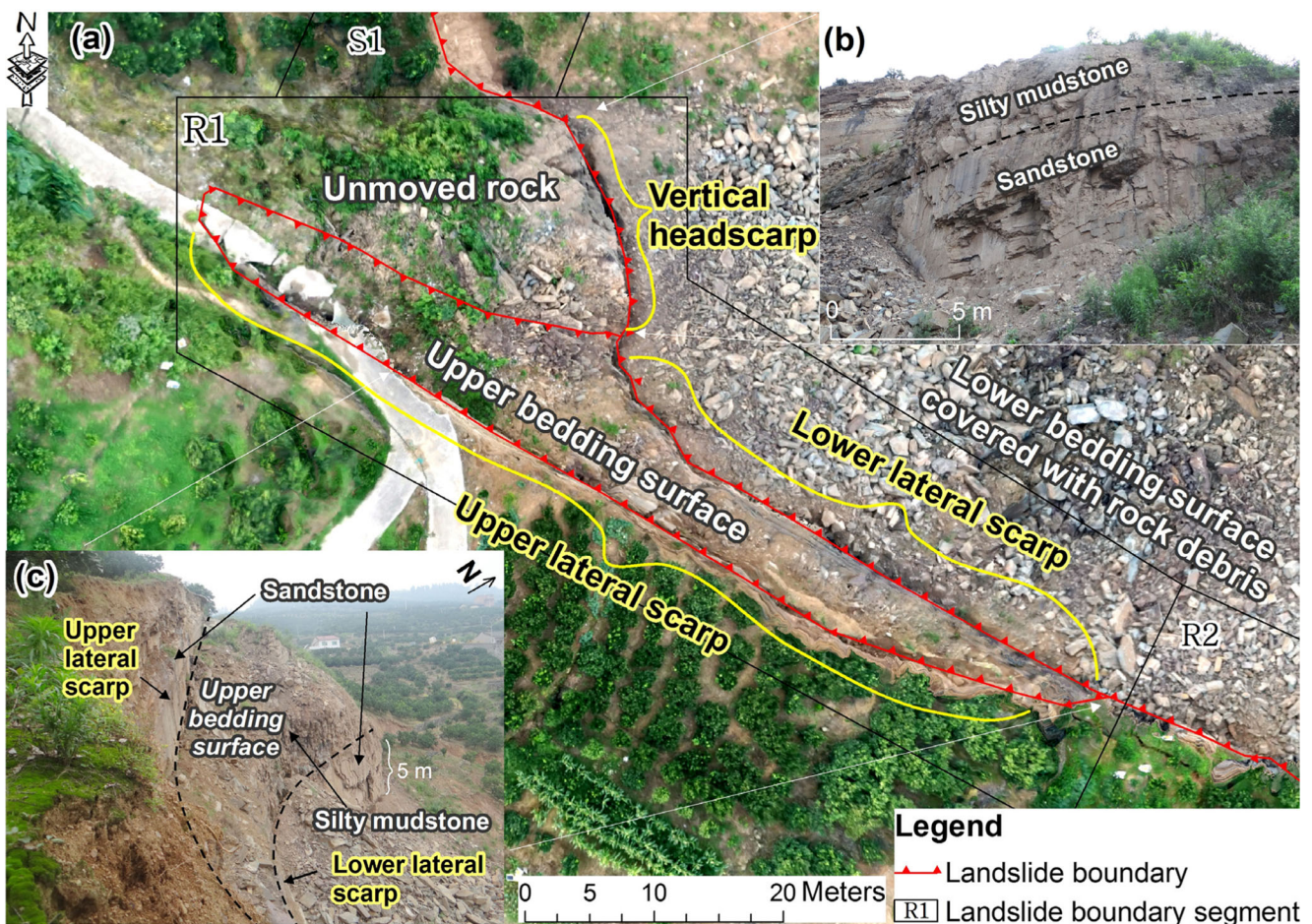
**Fig. 7** Features of segment R1 (in Fig. 6) of the Shanshucao landslide boundary; the base map is the micro-UAV based orthomosaic from June 19, 2015. **a** Overall view of R1; **b** vertical headscarp; and **c** double lateral scarps

## Landslide characteristics

### Landslide boundary

The landslide boundary was delineated accurately using post-landslide orthomosaics, especially the high-resolution micro-UAV based orthomosaic (Fig. 6).

The southern rocky part exhibited an obvious difference in color, texture, etc., on the orthomosaic; therefore, the southern boundary could be easily identified. Moreover, the borders had the following features.

- Vertical headscarp and double lateral scarps in the southwestern part (R1 in Fig. 6).

There were complicated head boundaries in the rocky part (Fig. 7a). First, a vertical headscarp approximately 10 m in height and 20 m in length was left in the northern area, and there was an unmoved rock mass in the west (Fig. 7b). Then, double lateral scarps were formed in the southwestern part: one was a lower lateral scarp, which was the extension of the northern vertical headscarp with

a length of approximately 46 m; the other was an upper lateral scarp, which lay on the southwestern outside area of the lower lateral scarp and was approximately 79 m in length. Accordingly, an upper bedding surface with an average width of approximately 6 to 7 m was formed between the double lateral scarps (Fig. 7c). Obviously, the complicated head boundaries were formed because two-tier sliding has occurred on the head of the rocky part, i.e., the vertical headscarp and lower lateral scarp were the result of the main deep sliding, whereas the upper lateral scarp was caused by secondary superficial sliding. In fact, the upper bedding surface was the superficial sliding surface.

Lithologically, the combination of the thick layered sandstones with interbedded thin to medium layered, silty mudstones could be observed on the scarp (Fig. 7b, c). Obviously, the soft silty mudstones were broken because of their weak anti-weathering ability, but the hard sandstones were the complete opposite. Moreover, the sliding surfaces formed easily along the interface between the upper sandstones and lower silty mudstones, e.g., both the lower bedding surface and upper bedding surface in Fig. 7 were sliding surfaces (Fig. 3).
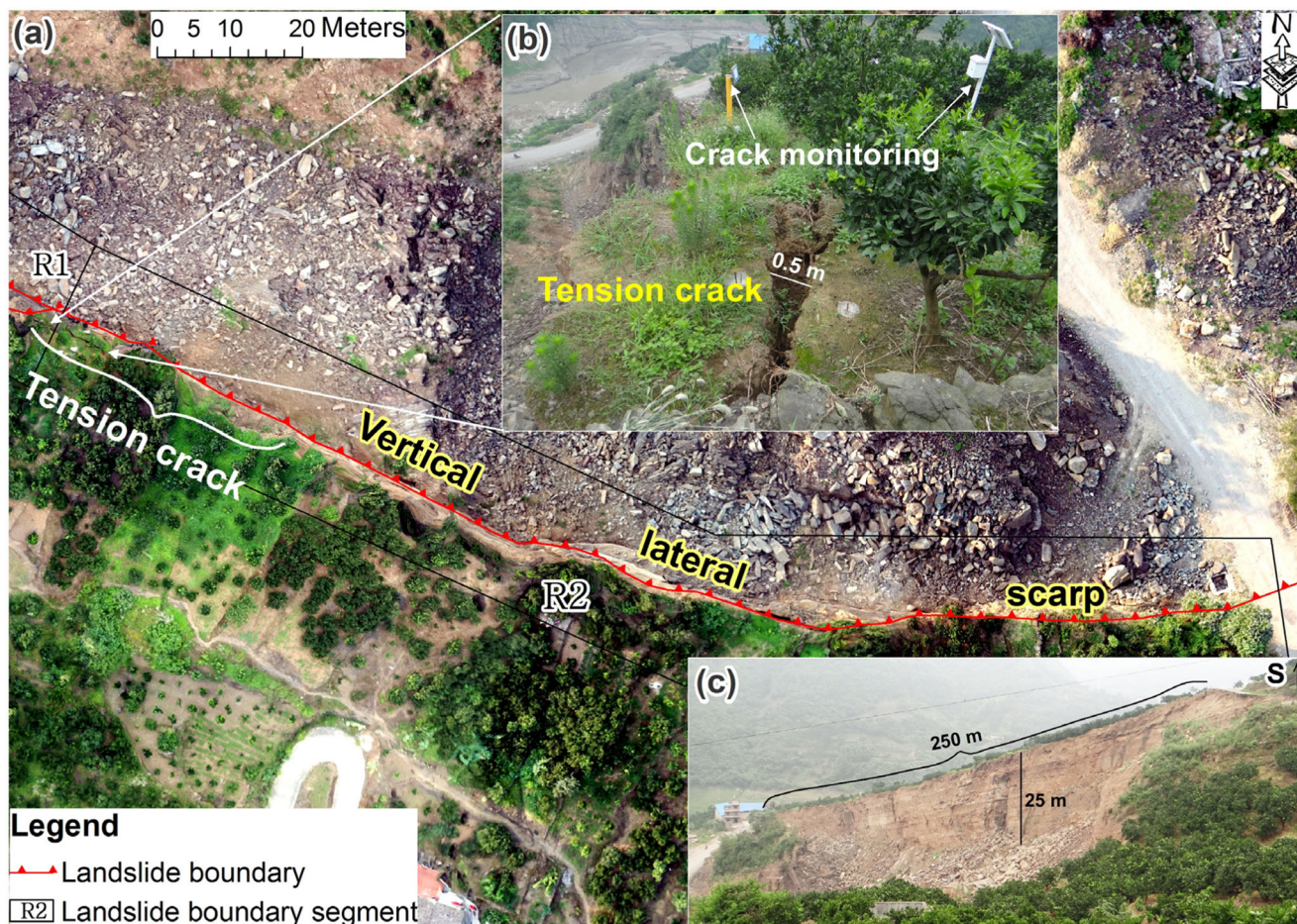
**Fig. 8** Features of segment R2 (in Fig. 6) of the Shanshucao landslide boundary; the base map is the micro-UAV based orthomosaic from June 19, 2015. **a** Overall view of R2; **b** tension cracks outside the boundary; and **c** vertical southern lateral scarp

- Vertical lateral scarp in the southern middle part (R2 in Fig. 6).

In R2, the upper and lower lateral scarps in R1 merged into a unified, vertical lateral scarp in the southern middle part (Fig. 8a, c), which implied that secondary superficial sliding occurred only in R1. The lateral scarp extended approximately 115 m along the azimuth of 116°, then turned to 90° and extended approximately 60 m to G348. In addition, a crack can be observed in the southern section of R2; the length was 39 m and the width exceeded 0.5 m, and it had the same extension direction as the lateral scarp. Crack-monitoring instruments were also installed (Fig. 8a, b).

- Grooved terrain in the southeastern part (R3 in Fig. 6).

Below G348, the features of the southern rocky boundary were obviously different from the vertical scarp above G348. A stable bedrock ridge gradually extended in the downstream direction of the Luogudong River, which hindered the sliding and led to a change in the sliding direction from east to northeast. Accordingly, when the high-speed sliding of the large

rocky mass was restricted by the bedrock ridge, the rocky mass was broken, and large amounts of fan-shaped cracks inevitably appeared (Fig. 9a). Along the boundary, in particular, the broken rocky mass uplifted due to the squeeze effect, and the grooved terrain was shaped (Fig. 9b). In addition, the rock debris and bedrock cliff can be easily identified on the banks of the Luogudong River (Fig. 9c).

In contrast, the northern soil part was hauled by the southern rocky mass, which led to the loose soil mass having inconsistent sliding directions and a shorter sliding distance than the southern part. Citrus trees were replanted on the soil mass, and thus the northern boundary could not be easily identified. Use of the micro-UAV based orthomosaic and field survey allowed for precise delineation of the northern soil part, and the features are as follows.

- Clear soil headscarp in the northwestern part (S1 in Fig. 6).

The soil headscarp could be divided into two parts (Fig. 8a): the southern part close to the rocky part had a slope of more than 60° and a height of approximately 3 m and was
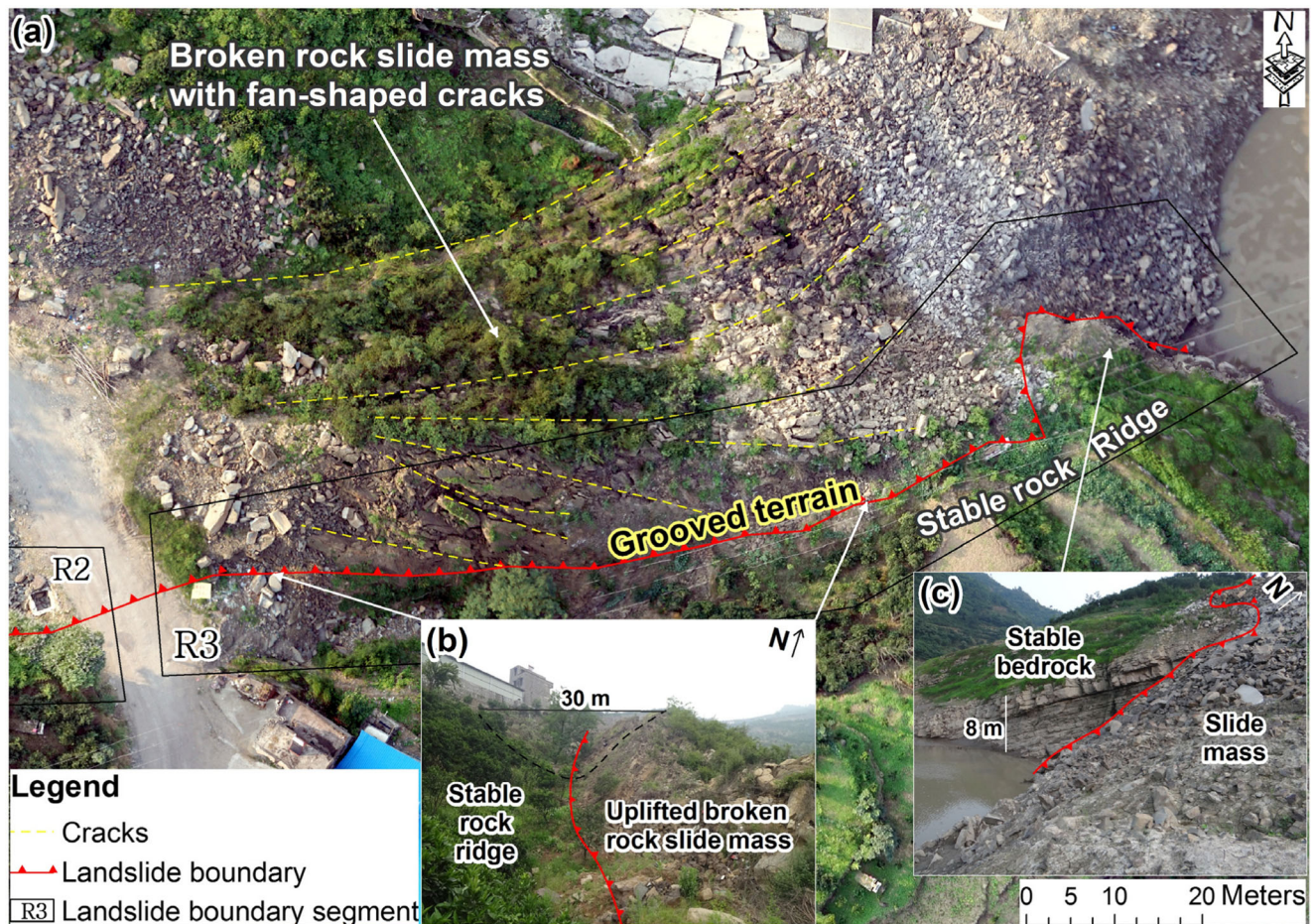
**Fig. 9** Features of segment R3 (in Fig. 6) of the Shanshucao landslide boundary; the base map is the micro-UAV based orthomosaic from June 19, 2015. **a** Overall view of R3; **b** grooved terrain; and **c** boundary on the river bank

positioned diagonally across three rows of staggered retaining walls (Fig. 10b); an approximately 4.5 m horizontal sliding distance with a 90° direction could be measured in this part. The northern headscarp had a gentle slope of approximately 40° and curved extension of approximately 110 m (Fig. 10c), which indicated an obvious difference from the steep and straight rocky mass boundary.

- Straight and hindered boundary between the soil and bedrock in the northern middle part (S2 in Fig. 6).

It was difficult to identify this part of the boundary based only on the orthomosaic because no obvious material collapse or lateral scarp could be found. By means of a field survey, the boundary was delineated. In contrast to the soil headscarp, bedrock could be found on the outside of the soil mass (Fig. 11a). The upper part of the boundary was formed by a straight crack (Fig. 11a, b). Even more interesting, the crack was not sheared but was tensional (Fig. 11b, c), which meant that this part might not have slid along the main direction, but instead,

it might have slid perpendicular to it. Whole bedrock lay across the middle, which hindered sliding and formed a concave boundary (Fig. 11d).

- Gully in the northeastern part (S3 in Fig. 6).

An obvious boundary was identified on the pavement of the G348 highway; the lateral retaining wall of G348 was pushed 13.6 m along the 109° direction of the sliding part (Fig. 12a, b). Below the highway, the boundary extended along a gully, and the stable bedrock lay on the northern part. In contrast, serious damage occurred in the landslide, e.g., a 5-story dormitory was destroyed. In addition, the bedrock that lay on the river bank protruded to the south, which hindered the sliding and changed its direction of movement (Fig. 12c).

### Landslide subzone

Based on the sliding distance and sliding mass material, the Shanshucao landslide could be divided into three subzones
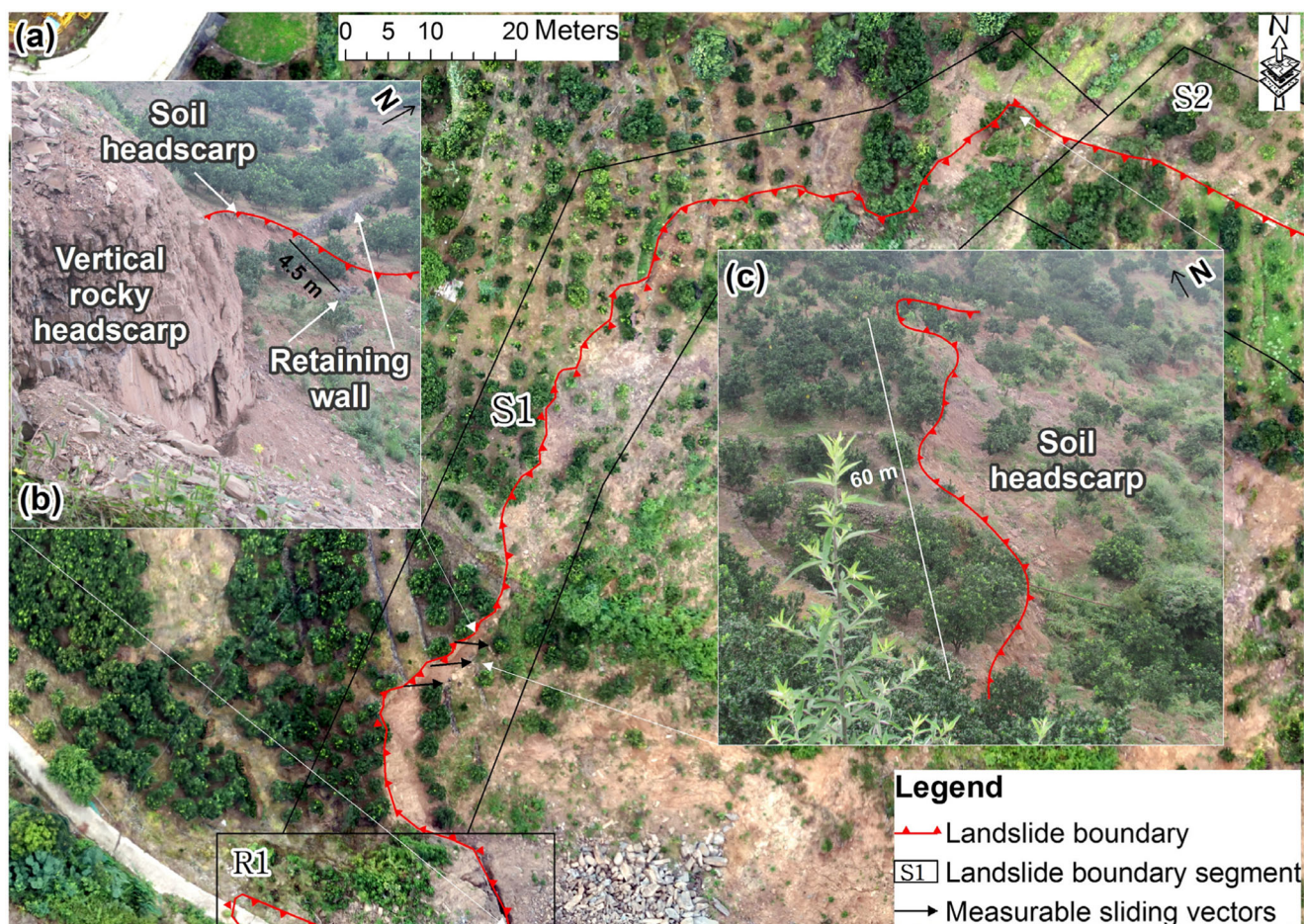
**Fig. 10** Features of segment S1 (in Fig. 6) of the Shanshucao landslide boundary; the base map is the micro-UAV based orthomosaic from June 19, 2015. **a** Overall view of S1; **b** southern steep soil headscarp; and **c** northern gentle soil headscarp

(Fig. 13): the main rock sliding zone (I), the main tractive soil sliding zone (II), and the secondary tractive soil sliding zone (III). This differs from other studies (Huang et al. 2015; Xu et al. 2015).

The main rock sliding zone (I in Fig. 13 b, c) moved significantly over a long distance, which resulted in a deep trough on the real surface and many broken rocks covered on the sliding surface (Figs. 3, 7). Accordingly, a residual rocky mass was left in the eastern area and was divided into two parts because of the re-excavation of the G348 highway; the western part became isolated, broken rocky cones with some living trees on top, the eastern part became a broken rock sliding mass with fan-shaped cracks on the back, and there was an obvious sliding tongue in the front riverbed.

According to the difference in materials and measurable sliding vectors, the boundary was delineated between zones I and II. In the western part of G348, a disturbed loose soil mass could be easily identified in zone II (Fig. 13 b). In the eastern part of G348, the impounding forebay moved 89–110 m along a 92–83° direction, while the retaining wall of G348 moved 14–21 m along a 110° direction, and the 5-story dormitory moved 4–12 m along a 77–96° direction; the

obvious difference meant that these objects lay in different zones (Fig. 13a, c). Moreover, in the satellite image of Dec. 17, 2014 obtained from Google Earth, the collapse of two large soil masses and a residual soil mass could be observed in the western part of G348 (Fig. 13b), which implied strong traction in zone II with the movement of zone I.

Similar to zone II, a soil mass covered zone III; however, there was smaller deformation in zone III because only a small collapse of the soil mass could be identified on the satellite image from Dec. 17, 2014 obtained from Google Earth (Fig. 13b). This implied that zone III was the secondary tractive soil sliding zone with the movement of zone II. Furthermore, on the orthomosaic captured by the UAV on June 19, 2015 (Fig. 13c), the boundary between zones II and III could not be identified because of the replanting of citrus trees.

### Altitude and volume change

Figure 14 shows the altitude change calculated from the difference between the DSM of the post-landslide area on June 19, 2015 and the DEM of the pre-landslide area in 2009.
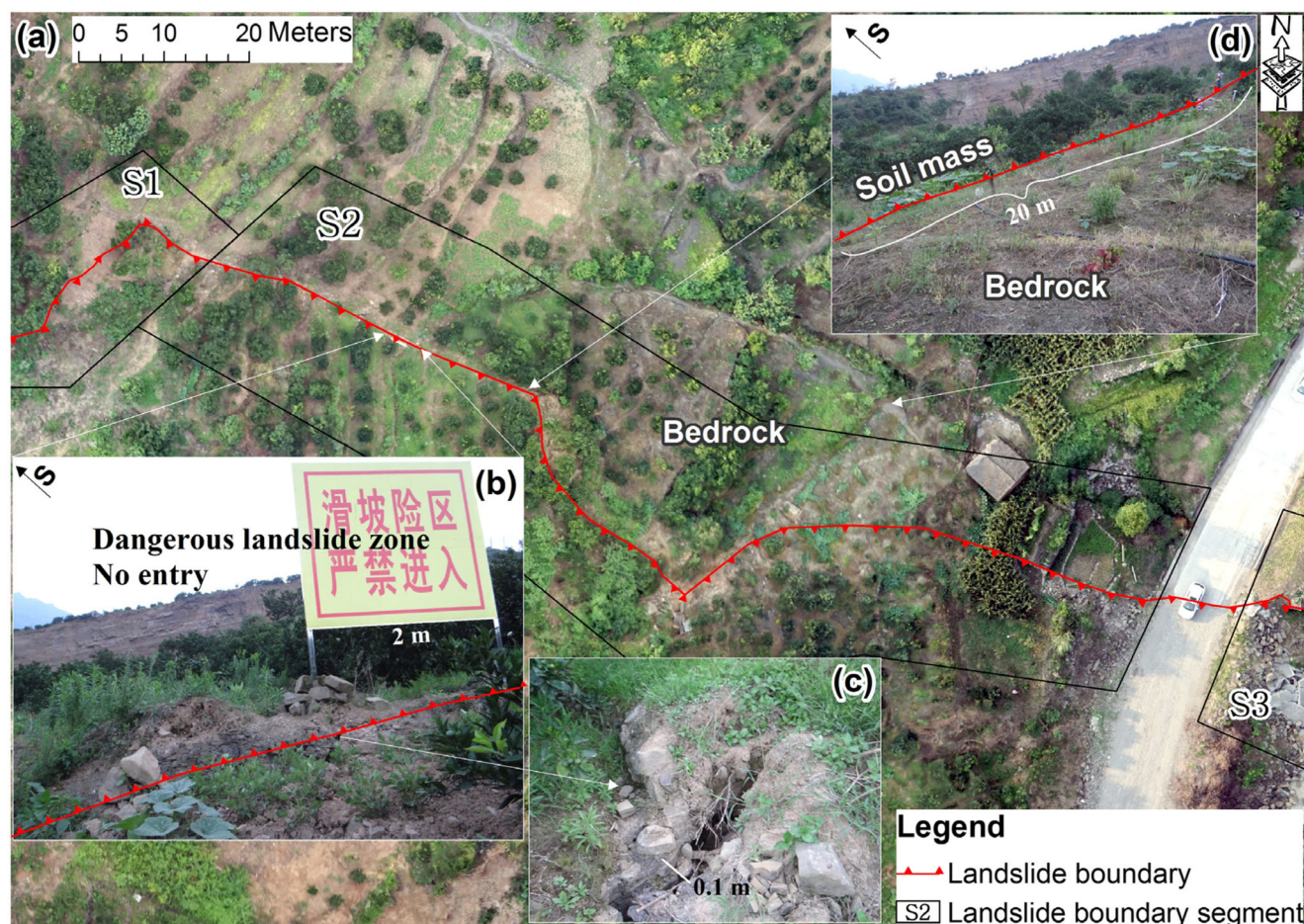
**Fig. 11** Features of segment S2 (in Fig. 6) of the Shanshucao landslide boundary; the base map is the micro-UAV based orthomosaic from June 19, 2015. **a** Overall view of S2; **b** straight crack boundary of the upper part; **c** tensional crack boundary; and **d** hindered boundary with bedrock in the lower part

The Shanshucao landslide led to a decrease in altitude and loss of material from the western part. Conversely, an increase in altitude and accumulation of material occurred in the eastern part. There were significant differences in the changes that occurred in the three zones (Table 3).

Obviously, the most significant change occurred in zone I, e.g., the maximum and average decrease in altitude reached 35.0 m and 14.4 m, respectively, while the average decrease in altitude was 2.7 m in zone II and 1.8 m in zone III. Similarly, the maximum and average increase in altitude was 22.3 m and 10.0 m in zone I, while the average increase in altitude was 2.1 m and 1.8 m in zones II and III, respectively.

The volume change showed that zone I was still the main sliding mass; the respective loss and accumulation volumes reached 141,371 m$^3$ and 141,623 m$^3$, while the respective loss and accumulation volumes were 13,732 m$^3$ and 13,920 m$^3$ in zone II and only 4087 m$^3$ and 4205 m$^3$ in zone III. The data presented in Table 3 are not accurate. This was because the real DEM could not be acquired from the UAV due to large tracts of cedar and citrus trees on the surface of the sliding mass; therefore, the DSM was used for the calculations (the

error was approximately 0.32 m, which is shown in Table 2). Nevertheless, the results could be used to imply some sliding laws.

There are two characteristics of terrain change in the area between pre- and post-landslide.

(1) The boundary between loss and accumulation gradually moved to the head in zones I, II, and III, which implied the longest sliding distance in zone I and the shortest in zone III. In other words, the sliding force changed significantly, i.e., decreasing gradually from southern zone I to northern zone III.

(2) There were two loss areas on the bank where the rocky sliding mass had passed through. This implied that the rocky sliding mass in zone I had considerable kinetic energy and even destroyed the bedrock ridge on both sides of the bank.

Overall, according to the change in the terrain in the area between pre- and post-landslide, the southern rocky sliding zone (zone I) was the main sliding zone with the longest
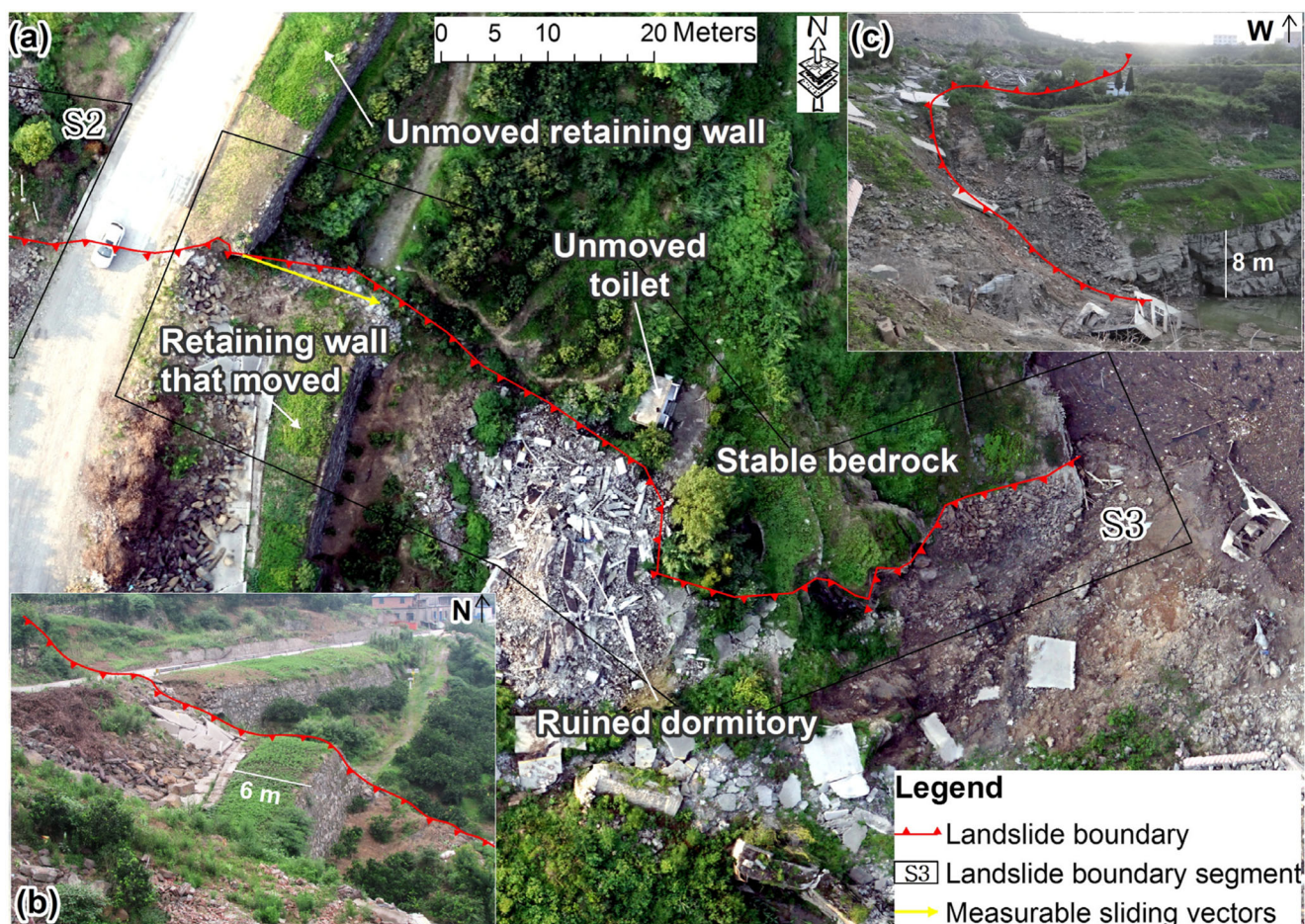
**Fig. 12** Features of segment S3 (in Fig. 6) of the Shanshucao landslide boundary; the base map is the micro-UAV based orthomosaic from June 19, 2015. **a** Overall view of S3; **b** obvious movement of highway pavement and retaining wall along the upper boundary; and **c** bedrock boundary on the river bank

distance and deepest sliding surface. Moreover, the rear section of the rocky sliding mass was reshaped into isolated, broken rocky cones because of re-excavation of the G348 highway (Fig. 15a), and a typical sliding tongue was formed on the front riverbed (Fig. 15b).

By contrast, the northern soil mass (zones II and III) had completely different deformation characteristics, i.e., no overall movement, but there was loose soil mass collapse. Moreover, under the traction of the southern rocky sliding mass, the deformation of zones II and III showed features of counterclockwise rotation, e.g., in zone II, the southern part had more obvious movement because of the traction of the southern rocky mass. This was similar in zone III, which was towed by zone II (Fig. 13b, c).

## Movement patterns

Based on the above analysis, the movement pattern of the Shanshucao landslide is presented in Fig. 16, and the following conclusions can be drawn:

(1) In zone I, the northern end of the concrete wall of the impounding forebay moved 89 m/92° (distance/azimuth) and the southern end moved 110 m/83° (the impounding forebay could be clearly distinguished on Fig. 13a at pre-landslide and on Fig. 13c at post-landslide). This implied the residual broken rocky cones should be the head part of the main rock sliding mass; therefore, the sliding distance of zone I was approximately 110 m. With respect to the sliding direction, the western part above the original impounding forebay slid along an average direction of 106°; the middle part, where the original impounding forebay extended to the river bank, showed the characteristics of forward extrusion, which extended from more than 90° to less than 80° under the bank block. In addition, when the sliding mass moved through the bank, the movement direction changed to 45°, and the eastern part formed a sliding tongue on the riverbed.

(2) In zone II below G348, the retaining wall moved 16–21 m along a direction of approximately 110°, whereas

Fig. 13 Three subzones of the
Shanshucao landslide. a
aerophotographic orthomosaic of
the pre-landslide area in 2009; b
satellite image of the post-
landslide area on Dec. 17, 2014,
which was obtained from Google
Earth; and c micro-UAV based
orthomosaic of the post-landslide
area on June 19, 2015
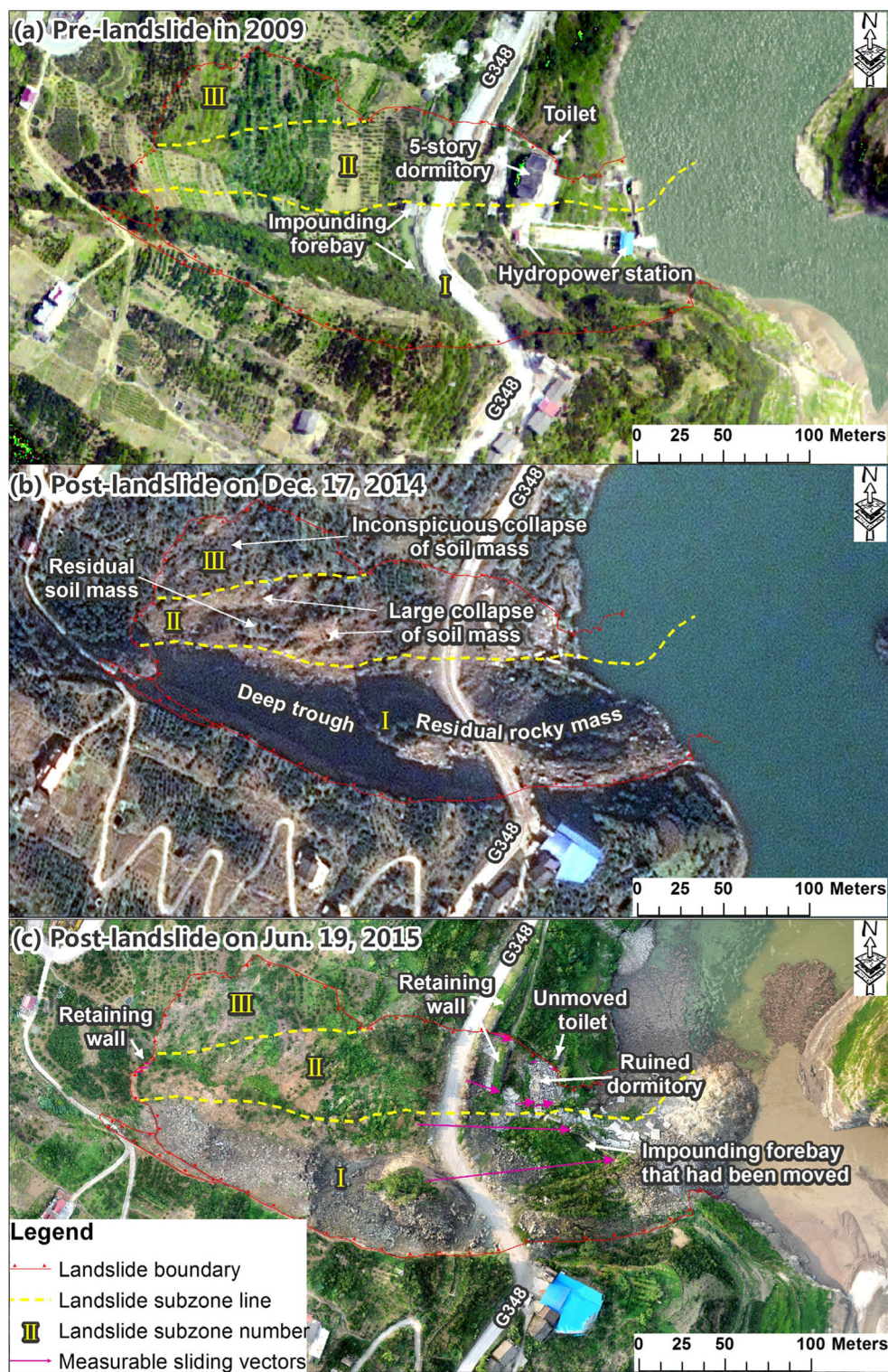


the 5-story dormitory was significantly affected by coun-
terclockwise thrust, which originated from both the trac-
tion of the southern rocky sliding mass and the block of
the eastern bedrock. This occurred because the directions
were between 77–83°, and the distance was shorter than

8 m along the northern boundary and 12–16 m along the
southern boundary; subsequently, the dormitory was
destroyed. Above G348, many soil ridges appeared be-
cause the thick and loose soil mass was towed and
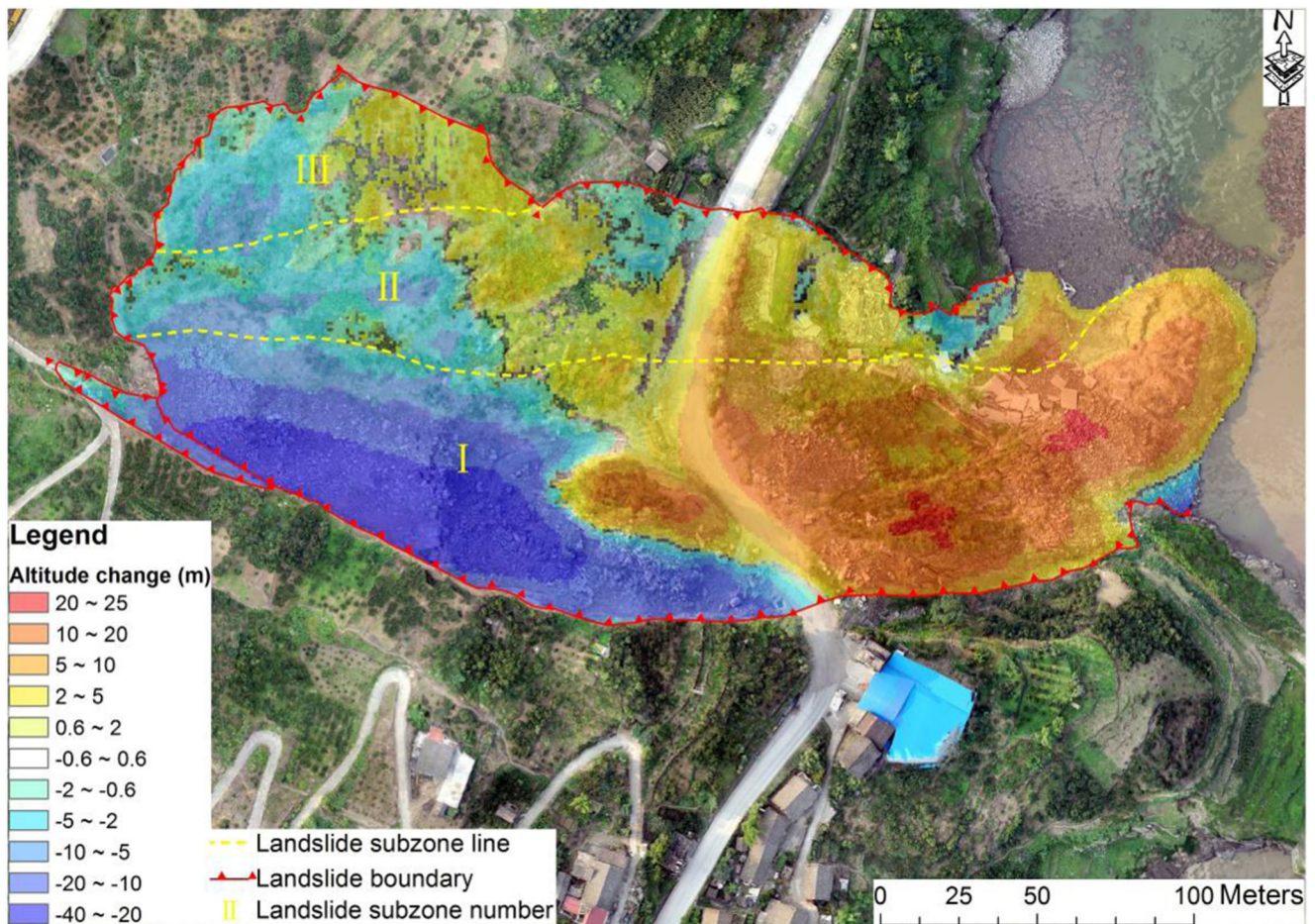moved counterclockwise. The collapse of two large soil

**Fig. 14** Altitude change between the pre- and post-landslide; the base map is the micro-UAV-based orthomosaic of June 19, 2015

masses was observed on both sides with a residual soil mass in the middle (Fig. 13 b).

(3) In zone III, under traction caused by zone II, the southern part had the farthest movement. Closer to the north with a short moving distance, the direction also gradually rotated counterclockwise simultaneously. Along the northern straight boundary, the upper soil mass and lower rocky bedrock were not obviously moved but were broken. This explained why the boundary crack was not sheared but was tensional (Fig. 11b, c). Therefore, to some extent, the bedrock along the northern boundary also played a blocking role in the slide.

## Discussion

### The lateral boundary of the rocky mass

When the exact boundaries of the post-landslide were superimposed on the aerophotographic orthomosaic and topographic contours of the pre-landslide area (Fig. 17), we observed that the overhanging rock cliff (Xu et al. 2015) that was approximately 20 m high and covered with cedar trees was actually located in the middle-upper part of the main rocky sliding mass, which was neither the southern boundary

**Table 3** Summary of altitude and volume changes in the area pre- and post-landslide

| Terrain change | | Landslide subzone | | |
|---|---|---|---|---|
| | | I | II | III |
| Altitude change (m) | Max. loss | 35.0 | 5.8 | 3.1 |
| | Avg. loss | 14.4 | 2.7 | 1.8 |
| | Max. accum. | 22.3 | 7.4 | 3.8 |
| | Avg. accum. | 10.0 | 2.1 | 1.8 |
| Area change (m$^2$) | Loss | 9792 | 5126 | 2278 |
| | Accum. | 14,203 | 6668 | 2747 |
| | Total | 23,995 | 11,794 | 5025 |
| Volume change (m$^3$) | Loss | 141,371 | 13,732 | 4087 |
| | Accum. | 141,623 | 13,920 | 4205 |
| | Total net | 252 | 188 | 118 |

**Fig. 15** Photos of the rear and front parts of the southern rocky sliding mass. **a** The residual broken rocky cones above G348 and **b** sliding tongue on the front riverbed

described in Wang and Yi (2015) nor the northern boundary described in Xu et al. (2015). The southern boundary of the post-landslide is evident as a lateral scarp with a length of more than 200 m and a height of more than 20 m (Figs. 7, 8), which meant researchers took for granted that the boundary had already existed for a long time; accordingly, the overhanging rock cliff that existed before the slide was easily mistaken for the southern boundary (Wang and Yi 2015). In practice, however, the actual southern boundary of the rocky mass was located on the southern side of the overhanging rock cliff. Meanwhile, the overhanging rock cliff was not the northern boundary of the rocky mass as described by Xu et al. (2015) because the impounding forebay that was located on the northern side also moved a long distance (Figs. 13, 16), i.e., the impounding forebay was still located on the rocky mass; therefore, there was no doubt that the actual northern boundary should pass through the northern side of the impounding forebay (Fig. 17). Field investigations showed that the overhanging
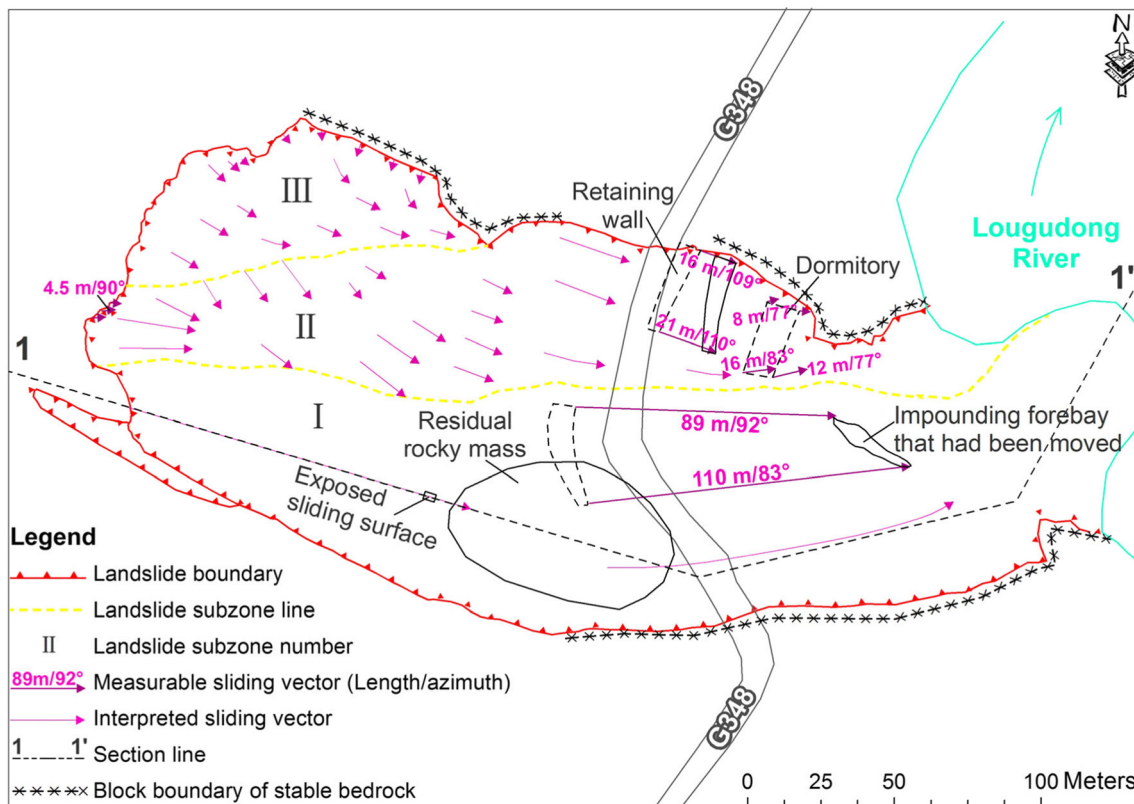


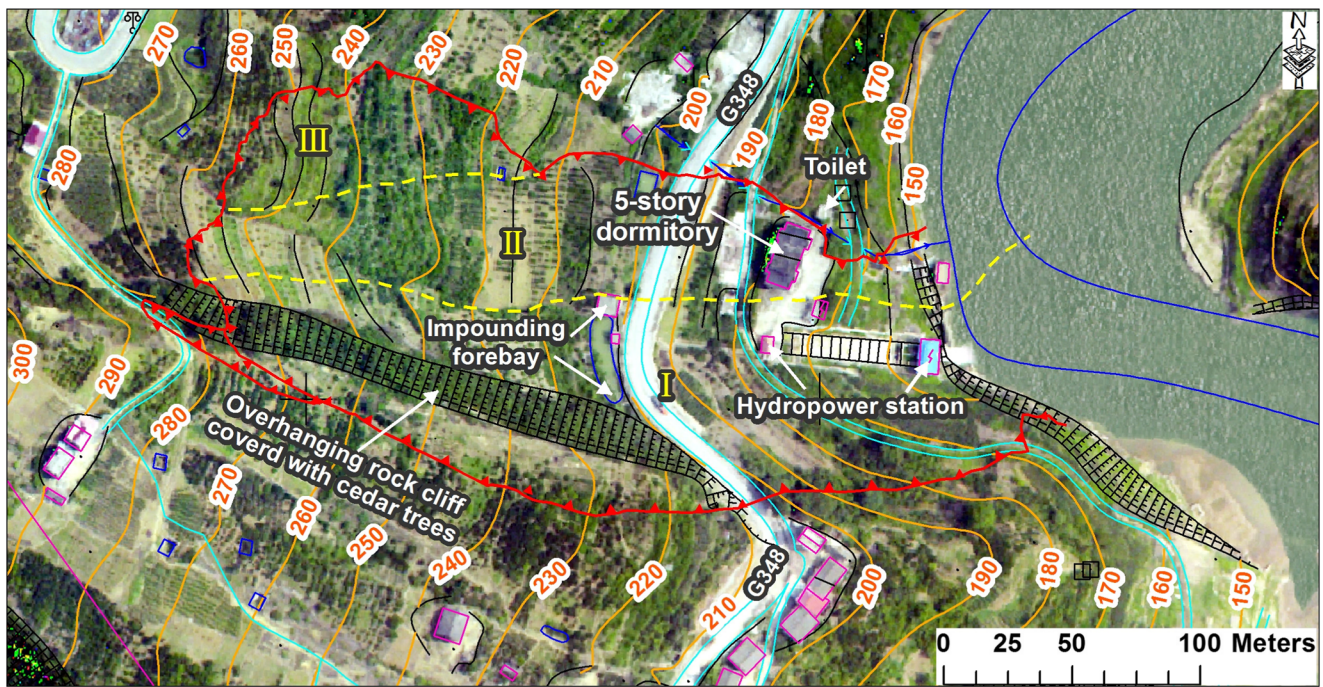**Fig. 16** The movement pattern of the Shanshucao landslide

**Fig. 17** The images and topographic contours of the pre-landslide area

rock cliff and the actual southern boundary belonged to the same set of tectonic fractures, the dip direction and dip angle of which were approximately 210–220°/80–90°; the only difference was that the boundary fracture extended into the citrus planting area, and no obvious topographic changes led to the lack of adequate attention. However, the rain marks and residual crack on the southern lateral scarp indicated that the southern boundary crack pre-existed, and its cutting depth was even greater than the height of the overhanging rock cliff (Fig. 18). At the same time, another set of tectonic fractures with the dip direction and dip angle of approximately 70–85°/86° formed the headscarp of the rocky mass.

## The shear outlet altitude and main trigger factors of rocky sliding

The exact location of the shear outlets for the rocky sliding can be used to determinate the accurate characteristics of the slide (e.g., length, area), as well as help understand the failure mechanism (e.g., whether it was affected by river water uplift). Undoubtedly, the shear outlets were in the left bank of the Luogudong River, which was originally a rock cliff (Fig. 17). However, the shear outlets were submerged below the water surface of the river before sliding and were then covered by landslide material after sliding. Thus, the altitude of the shear
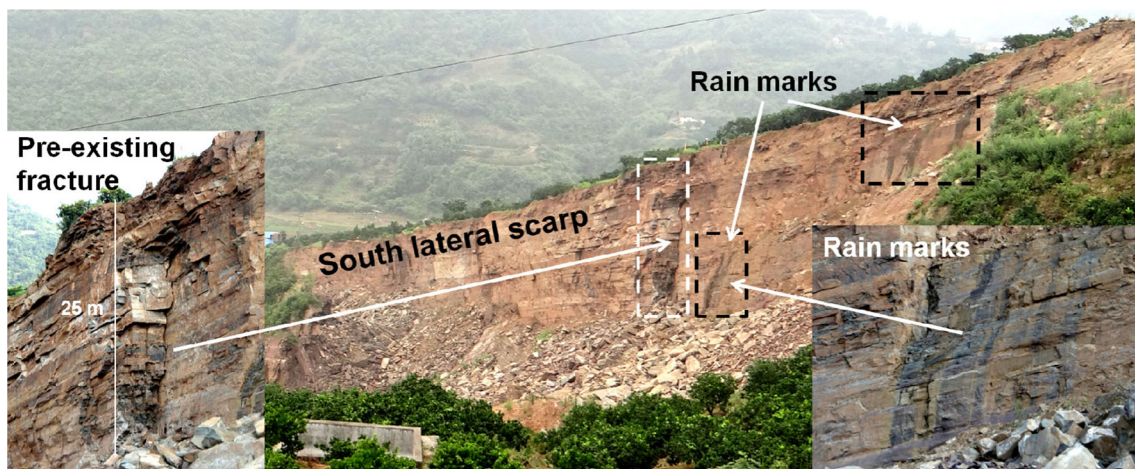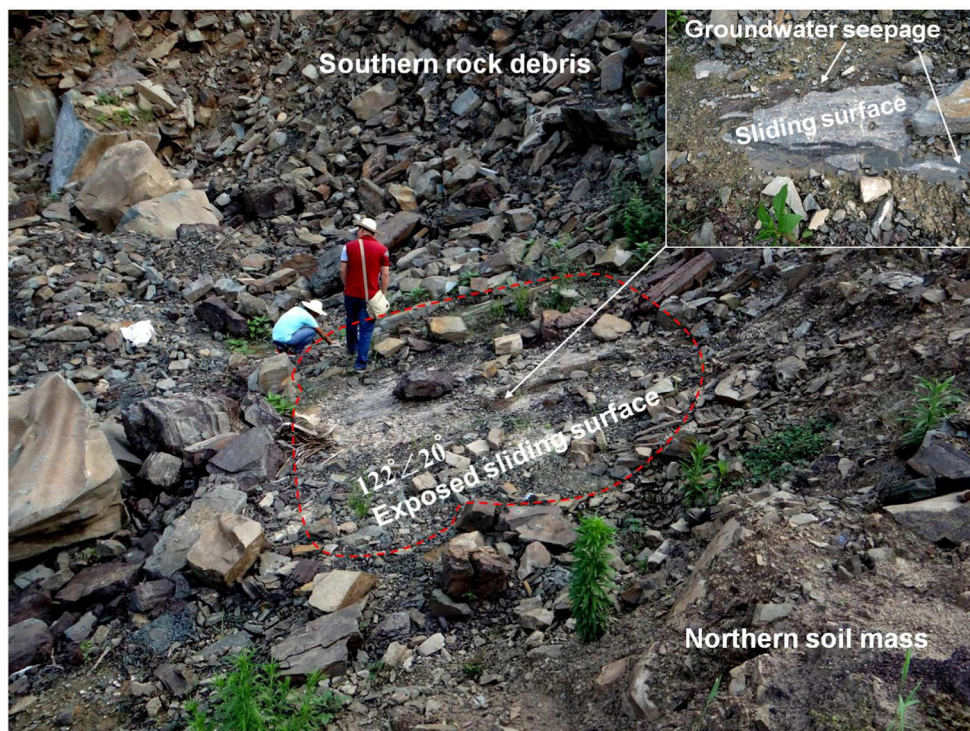


**Fig. 18** The rain marks and residual crack on the south lateral scarp

**Fig. 19** The exposed sliding surface of the rocky landslide



outlets was unknown, and no direct evidence could be found in the field.

Figure 15a shows that the residual broken rocky mass and the southern lateral scarp were in complete agreement with the original sediments and occurrence, which indicated that the rocky sliding was a typical translational movement, and this has been recognized in Huang et al. (2015), Wang and Yi (2015), and Xu et al. (2015). Therefore, if some true sliding surfaces could be found in the landslide body, the accurate shear outlet altitude could be deduced by the position and the unchangeable occurrence of the sliding surface. Fortunately, one such exposed smooth sliding surface with an area of approximately 10 m$^2$ was found in the rock debris accumulation (Fig. 19); the lithology was silty mudstone, and the dip direction and dip angle were 122°/20°. Accordingly, based on the terrain of the area pre- and post-landslide and the exposed sliding surface, the longitudinal section sketch of the rocky sliding mass could be concluded as presented in Fig. 3. The altitude of shear outlets was 145.6 m, which is consistent with the result reported in Xu et al. (2015), while the 180 m reported by Huang et al. (2015) is an obvious error.

From Fig. 3, some characteristics of the rocky mass could be accurately measured, e.g., the whole rock mass was 329 m long, and the sliding distance was 120 m (therefore, 160 m in Xu et al. (2015) was clearly overestimated).

With respect to the triggering factors of the rocky sliding, the leakage of the tunnel pipelines was considered a key factor, and the intense rain and rapid increase in the water level of the river were considered secondary factors in Huang et al. (2015). However, in Xu et al. (2015), both the heavy rain and increase in the water level were the key factors, neither of which could be neglected.

Indeed, the intense rain and rapid increase in the water level of the river were two major external trigger factors that must be considered, especially for landslides in the Three Gorges Reservoir (Wang et al. 2004; Huang et al. 2014; Jian et al. 2014). There were abnormal changes in these factors prior to the Shanshucao landslide, i.e., cumulative rainfall within 33 days reached 331.9 mm, and rainfall on the day of the sliding reached 96.5 mm. In addition, the water level of the river increased by 4.8 m within 36 h before the sliding; these changes were significantly higher than the typical values (Huang et al. 2014; Xu et al. 2015). The failure of the landslide was triggered by both the intense rainfall and the rapid increase in the water level of the river; however, we believed that the importance of these two factors differed. According to Fig. 3, the water level of the river increased from 158.2 m at 2:00 on Sept. 1 to 162.8 m at 14:00 on Sept. 2, 2014 (i.e., the moment when the landslide occurred). The rate at which the water level increased was indeed higher than the average value; however, the volume of the newly increased, submerged slide caused by the water level rise of 4.8 m accounted for less than 2% of the whole landslide volume, which meant that the uplift pressure at the front of the landslide caused by the increase in the reservoir water level should have

been very limited. However, this was only an empirical judgment, we could not be entirely sure.

On the other hand, according to the field survey, a slight amount of groundwater seepage was observed at the position where the exposed sliding surface was in contact with the overlying rock debris (Fig. 19). As the level of the original groundwater was low on the slope, the observed groundwater could only originate from the rainwater that infiltrated into the sliding mass and then flowed along the sliding surface. Therefore, two sets of tectonic fractures that pre-existed and were extremely developed provided many channels for rainfall infiltration (similar to the rain marks on the southern lateral scarp in Fig. 18), and the mudstone layers became the confining bed. The sliding surface became the impervious base of the channel through which the infiltrated groundwater flowed into the river. Under conditions of continuous heavy rain, a large amount of rainwater infiltrated into the landslide mass along two sets of tectonic fractures. Additionally, the groundwater discharged very slowly along the pelitic sliding surface, a large thrust was generated in the vertical fractures (i.e., the headscarp and southern lateral scarp after the sliding), and uplift pressure was generated above the sliding surface; both of these processes became the primary forces that triggered the sliding. In addition, the sliding surface formed by the mudstone was softened by the groundwater over a long period, which led to a considerable decrease in the shear strength (Stark et al. 2005; Xu et al. 2015) and then further aggravated the sliding. In summary, we believe, with reservations, that rainfall was the key trigger of the rocky sliding. To clarify the mechanism of the Shanshucao landslide, numerical simulation analysis of the rainfall impact, increase in river water, and leakage of tunnel pipelines is currently underway.

## Conclusions

As a typical landslide that occurred in the Three Gorges Reservoir area in recent years, the Shanshucao landslide has received considerable attention. To better understand the movement characteristics and patterns of the sudden landslide, three periods of multi-source remote sensing images were used and combined with a field survey. The conclusions of this study are presented as follows.

1. The landslide boundary was accurately delineated by using post-landslide orthomosaics, especially a high-resolution micro-UAV based orthomosaic with the field survey; therefore, more detailed characteristics were described. First, in the rocky part, there were complicated head boundaries with a vertical headscarp and double lateral scarps, which implied that two-tier sliding occurred in this area. Subsequently, the southern double lateral scarps merged into a unified, vertical lateral scarp and changed direction from southeast to east. Below G348, due to the blockage, the direction of the boundary continued to change to the northeast, and significant fan-shaped cracks were formed on the broken rocky mass. Second, clear soil headscarps were also present in the soil, but insignificant tension rather than a sheared fracture boundary occurred in the upper part, and then, the boundary extended along a gully to the river bank in the lower part.

2. Three subzones of the landslide were identified, i.e., the main rock sliding zone (I), the main tractive soil sliding zone (II), and the secondary tractive soil sliding zone (III). Different from previous studies, the two boundaries between the three subareas were more precisely divided based on a comparison of images of the pre- and post-landslide area.

3. Combined with the quantified changes in altitude and volume between the pre- and post-landslide, a movement pattern could be proposed, i.e., the southern rocky sliding part (zone I) was the main sliding zone with the longest distance and the deepest sliding surface, and its sliding direction gradually changed from southeast (i.e., 106°) to northeast (i.e., 45°) under the block of the south bedrock ridge and river bank. The northern soil mass (zones II and III) did not experience overall movement, but loose soil mass collapse and features of counterclockwise rotation were observed under the traction of the southern rocky sliding. Moreover, because of the direct traction of the rapid sliding of the rock mass, zone II showed more obvious soil damage than zone III, which was only towed by zone II.

In addition, more accurate knowledge about this process had been obtained as follows.

1. The pre-existing, overhanging rock cliff that was approximately 20 m high and covered with cedar trees was located in the middle-upper part of the main rocky sliding mass, which was neither the southern nor northern boundary.

2. The altitude of the shear outlets located on the left bank of the Luogudong River was 145.6 m; the whole rock mass was 329 m long and the sliding distance was 120 m.

3. Rainfall was believed to be the key triggering factor of the rocky sliding, with reservations; however, verification of this requires more accurate quantitative analysis.

# References

Carlà T, Farina P, Intrieri E, Botsialas K, Casagli N (2017) On the monitoring and early-warning of brittle slope failures in hard rock masses: examples from an open-pit mine. Eng Geol 228:71–81. https://doi.org/10.1016/j.enggeo.2017.08.007

Chung MC, Tan CH, Chen CH (2016) Local rainfall thresholds for forecasting landslide occurrence: Taipingshan landslide triggered by Typhoon Saola. Landslides 14(1):19–33. https://doi.org/10.1007/s10346-016-0698-2

Colomina I, Molina P (2014) Unmanned aerial systems for photogrammetry and remote sensing: a review. ISPRS J Photogramm Remote Sens 92:79–97. https://doi.org/10.1016/j.isprsjprs.2014.02.013

De Novellis V, Castaldo R, Lollino P, Manunta M, Tizzani P (2016) Advanced three-dimensional finite element modeling of a slow landslide through the exploitation of DInSAR measurements and in situ surveys. Remote Sens 8(8):670. https://doi.org/10.3390/rs8080670

Huang H, Yi W, Lu S, Yi Q, Zhang G (2014) Use of monitoring data to interpret active landslide movements and hydrological triggers in three gorges reservoir. J Perform Constr Facil 30(1):C4014005. https://doi.org/10.1061/(asce)cf.1943-5509.0000682

Huang B, Zheng W, Yu Z, Liu G (2015) A successful case of emergency landslide response - the Sept. 2, 2014, Shanshucao landslide, three gorges reservoir, China. Geoenvironmental Disasters 2(1):1–9. https://doi.org/10.1186/s40677-015-0026-5

Huang H, Long J, Lin H, Zhang L, Yi W, Lei B (2017a) Unmanned aerial vehicle based remote sensing method for monitoring a steep mountainous slope in three gorges reservoir, China. Earth Sci Inf 10(3): 287–301. https://doi.org/10.1007/s12145-017-0291-9

Huang H, Long J, Yi W, Yi Q, Zhang G, Lei B (2017b) A method for using unmanned aerial vehicles for emergency investigation of single geo-hazards and sample applications of this method. Nat Hazards Earth Syst Sci 17(11):1961–1979. https://doi.org/10.5194/nhess-2017-44

Immerzeel WW, Kraaijenbrink PDA, Shea JM, Shrestha AB, Pellicciotti F, Bierkens MFP, Jong SMD (2014) High-resolution monitoring of Himalayan glacier dynamics using unmanned aerial vehicles. Remote Sens Environ 150(7):93–103. https://doi.org/10.1016/j.rse.2014.04.025

Jian W, Xu Q, Yang H, Wang F (2014) Mechanism and failure process of Qianjiangping landslide in the three gorges reservoir, China. Environ Earth Sci 72(8):2999–3013. https://doi.org/10.1007/s12665-014-3205-x

Kasperski J, Delacourt C, Allemand P, Potherat P, Jaud M, Varrel E (2010) Application of a terrestrial laser scanner (TLS) to the study of the Séchilienne landslide (Isère, France). Remote Sens 2(12): 2785–2802. https://doi.org/10.3390/rs2122785

Lucieer A, Jong SMD, Turner D (2014) Mapping landslide displacements using structure from motion (SfM) and image correlation of multitemporal UAV photography. Prog Phys Geogr 38(1):97–116

Macciotta R, Hendry M, Martin CD (2016) Developing an early warning system for a very slow landslide based on displacement monitoring. Nat Hazards 81(2):887–907. https://doi.org/10.1007/s11069-015-2110-2

Manconi A, Giordan D (2016) Landslide failure forecast in near-real-time. Geomat Nat Haz Risk 7(2):639–648. https://doi.org/10.1080/19475705.2014.942388

Martha TR, Kerle N, Jetten V, van Westen CJ, Kumar KV (2010) Landslide volumetric analysis using cartosat-1-derived dems. IEEE Geosci Remote Sens Lett 7:582–586

Niethammer U, James MR, Rothmund S, Travelletti J, Joswig M (2012) UAV-based remote sensing of the super-Sauze landslide: evaluation and results. Eng Geol 128:2–11. https://doi.org/10.1016/j.enggeo.2011.03.012

Petley DN, Bulmer MH, Murphy W (2002) Patterns of movement in rotational and translational landslides. Geology 30(8):719–722. https://doi.org/10.1130/0091-7613

Stark TD, Choi H (2008) Slope inclinometers for landslides. Landslides 5(3):339–350. https://doi.org/10.1007/s10346-008-0126-3

Stark TD, Choi H, McCone S (2005) Drained shear strength parameters for analysis of landslides. J Geotech Geoenviron 131(5):575–588

Tofani V, Segoni S, Agostini A, Catani F, Casagli N (2013) Technical note: use of remote sensing for landslide studies in Europe. Nat Hazards Earth Syst Sci 13(2):299–309. https://doi.org/10.5194/nhess-13-299-2013

Turner D, Lucieer A, de Jong S (2015) Time series analysis of landslide dynamics using an unmanned aerial vehicle (UAV). Remote Sens 7(2):1736–1757. https://doi.org/10.3390/rs70201736

Wang M, Yi W (2015) Geological characteristics and formation mechanism of Shanshucao landslide in three gorges reservoir area. J Chin Three Gorges Univ (Nat Sci) 37(05):44–47. https://doi.org/10.13393/j.cnki.issn.1672-948X.2015.05.011 (in Chinese)

Wang F, Zhang Y, Huo Z, Matsumoto T, Huang B (2004) The July 14, 2003 Qianjiangping landslide, three gorges reservoir, China. Landslides 1:157–162. https://doi.org/10.1007/s10346-004-0020-6

Westoby MJ, Brasington J, Glasser NF, Hambrey MJ, Reynolds JM (2012) 'Structure-from-motion' photogrammetry: a low-cost, effective tool for geoscience applications. Geomorphology 179:300–314. https://doi.org/10.1016/j.geomorph.2012.08.021

Xu G, Li W, Yu Z, Ma X, Yu Z (2015) The 2 September 2014 Shanshucao landslide, three gorges reservoir, China. Landslides 12(6):1169–1178. https://doi.org/10.1007/s10346-015-0652-8